RSC Advances

ROYAL SOCIETY OF CHEMISTRY

www.rsc.org/advances

Journal Name

ARTICLE

Received 00th January 20xx,
Accepted 00th January 20xx

DOI: 10.1039/x0xx00000x

www.rsc.org/

High dielectric constant and capacitance in ultrasmall (2.5 nm) $SrHfO_3$ perovskite nanoparticles produced from a low temperature non-aqueous sol-gel route

Mohamed Karmaoui,[a,b*] E.Venkata Ramana,[c] David M. Tobaldi,[a] Luc Lajaunie,[d] Manuel. P. Graça,[c] Raul Arenal,[d,e] Maria P. Seabra,[a] João A. Labrincha[a] and Robert C. Pullar[a*]

ABSTRACT: Strontium hafnium oxide ($SrHfO_3$) has great potential as a high-k gate dielectric material, for use in memories, capacitors, CMOS and MOSFETs. We report for the first time the dielectric properties (relative permittivity and capacitance) of $SrHfO_3$ nanoparticles (NPs), as opposed to thin films or sintered bulk ceramics. These monodisperse, ultra-small, perovskite-type $SrHfO_3$ nanocrystals were synthesised through a non-aqueous sol-gel process under solvothermal conditions (at only 220 ^{o}C) using benzyl alcohol as a solvent, and with no other capping agents or surfactants. Advanced x-ray diffraction methods (whole powder pattern modelling, WPPM), CS-corrected high-resolution scanning transmission electron microscopy (HRSTEM), dielectric spectroscopy, and optical (UV-vis, Raman) and photoluminescent spectroscopy were used to fully characterize the NPs. These $SrHfO_3$ NPs are the smallest reported and highly monodisperse, with a mean diameter of 2.5 nm, a mode of 2.0 nm and a small size distribution. The formation mechanism of the NPs was determined using NMR and GC-MS analysis of the species involved. Our $SrHfO_3$ nanoparticles had a dielectric constant of 17, which is on par with literature data for bulk and thin film samples, and they also had a relatively large capacitance of 9.5 nF cm^{-2}. As such, they would be suitable for applications as gate dielectrics for capacitors and in metal-oxide semiconductor field-effect transistor (MOSFET) technology.

[a] *Department of Materials and Ceramic Engineering / CICECO – Aveiro Institute of Materials, University of Aveiro, Campus Universitário de Santiago, 3810-193 Aveiro, Portugal *E-mail: rpullar@ua.pt ; karmaoui@ua.pt ; Tel: +351 234 370 041*
[b] *School of Chemistry, College of Engineering and Physical Sciences, University of Birmingham, Edgbaston, Birmingham, B15 2TT , UK *Email: m.karmaoui@bham.ac.uk; Tel: +44 121 414 8672*
[c] *I3N-Aveiro, Department of Physics, University of Aveiro, Campus Universitário de Santiago, 3810-193 Aveiro, Portugal.*
[d] *Laboratorio de Microscopías Avanzadas, Instituto de Nanociencia de Aragón, Universidad de Zaragoza, 50018 Zaragoza, Spain.*
[e] *ARAID Foundation, 50018 Zaragoza, Spain.*

Electronic Supplementary Information (ESI) available: ^{13}C NMR spectrum ^{1}H NMR spectrum, Gas chromatogram, Retention times and structures of relevant organic species and WPPM agreement factors, unit cell parameters, average crystalline domain diameter, and mode of the size distribution.

Of the various classes of inorganic nanoparticles (NPs), perovskite metal oxides NPs are particularly attractive from both the scientific and technological point of view. The unique characteristics of perovskites make them the most diverse class of materials for use in electronics and fuel cells due to their optimal optical, dielectric, ferroelectric, piezoelectric, photoelectric, catalytic or magnetic properties.[1-10] Recently, much interest has been focused on the synthesis and characterization of multi-metal oxide NPs, and significant progress has been made over the last decade in understanding fundamental aspects of the synthesis of perovskite nanomaterials. Of these functional oxides, extensive work is available on $BaTiO_3$ (BTO) and $SrTiO_3$ (STO) based nanomaterials as their size-induced effects can be used to adjust dielectric and ferroelectric properties. A perovskite-type strontium hafniate ($SrHfO_3$) nanomaterial has also recently attracted a lot of attention due to its promising electrical and optical properties. $SrHfO_3$ doped with various ions (particularly Ce and Cu) is established as good luminescent material and scintillating materials for use in high energy nuclear medical applications .[11] However, to date, little work has been reported on the synthesis and physical properties of $SrHfO_3$ NPs, is in contrast to the much-studied BTO and STO nanomaterials.[7-10] What work has been carried out on nanoscale $SrHfO_3$ is nearly all on thin films [12], for high-k gate dielectric transistors [13] and photoluminescent properties.[4]

Alkaline earth hafniates have great potential as near-zero τ_f microwave dielectric ceramics,[14] and in particular $SrHfO_3$ is a very promising candidate for the next generation of capacitors, complementary metal–oxide–semiconductor (CMOS)[10] and metal-oxide-semiconductor-field-effect-transistor (MOSFET) devices,[15] due to its outstanding physical and electrical properties. It possesses a dielectric constant (k) of 21, a semiconductor band gap (E_g) of 6.1 eV, and a lower gate leakage current, superior to that of STO (E_g = 3.4 eV).[16] Thin films of $SrHfO_3$ were found to be good materials with equivalent oxide thickness (EOT) < 1 nm and reasonable channel mobility. In n-type field effect transistor (n-FETs) fabricated from $SrHfO_3$, Rossel *et al*.[17] observed an increase in channel mobility with post processing annealing at 150 °C. However, thin films of $SrHfO_3$ have been seen to have lowered photoconductivity thresholds of 4.5-5.7 eV, suggesting they are separating into HfO_2 and SrO oxides.[18] van Loef *et al.* reported that Ce-doped $SrHfO_3$ ceramics yielded greater enhancement in radio luminescence, with values four orders of magnitude greater when compared to conventional materials used in scintillator applications.

Apart from these applications, $SrHfO_3$ also shows different temperature-dependent phase transitions at high temperatures. From room temperature (300 K) to 673 K, $SrHfO_3$ displays the orthorhombic (*Pbnm*) form. It transforms to another orthorhombic phase, (*Cmcm*), somewhere in the range 673-873 K, consisting entirely of the orthorhombic (*Cmcm*) form at 873 K. At 1023 K, SrHfO3 is transformed in to the tetragonal (I4/mcm) which remains stable up to 1353 K, and this has transformed into the cubic (Pm3m) phase at 1403 K, an undistorted cubic perovskite structure.[16] High temperature Raman studies have shown that the 1023 K phase transition is displacive, with no disorder involved, and nearly second-order, which could affect the subsequent electrical properties of annealed $SrHfO_3$ thin films.[19] These phases are not stable upon cooling, and revert to their previous structures, yielding the (*Pbnm*) phase when cooled down to room temperature again. A ferroelectric soft mode has been observed by means of Raman spectroscopy,[19] and $SrHfO_3$ also has interesting optical properties.[19, 20]

Various processing routes have been developed for the synthesis and characterization of different perovskite-type NPs, such as coprecipitation,[20, 21] the citrate process,[22] sol-gel chemistry,[23] solid state methods,[24] hydrothermal synthesis[25] and solvothermal processing.[26]

However, there has been very little work on the synthesis of $SrHfO_3$ NPs, partly because of the high temperature required. $SrHfO_3$ requires prolonged calcination at 1100-1200◦C for several hours [27], often along with inter-mediate grinding [28] to form in solid-state reactions, with large consequential grain growth, and requires even higher temperatures of 1600-1750 °C to be sintered. [29] Even in thin film form, is a need to be annealed at 650-800 °C to become crystalline. [15] Pure and doped $SrHfO_3$ NPs have been formed by combustion synthesis, and Ce-doped $SrHfO_3$ has been made by sol-gel synthesis for possible use in laser and scintillator applications, but even though these required lower temperatures in some cases, the smallest NPs produced were still 40 nm. [29] 10-20 nm $SrHfO_3$ NPs were made by a complex process using hafnium metallocenes and strontium alkoxides, but a synthesis temperature of 800 °C was still required.[30]

Hydrothermal and solvothermal methods are particularly useful for producing perovskite NPs at lower temperatures, and they can be applied to synthesize broad classes of NPs, while controlling particle size and morphology. Large (100nm-1 μm) hollow cuboids of $SrHfO_3$ have been produced from hydrothermal synthesis at 200 °C, and their photoluminescent spectra investigated. [31] However, one of the main challenges for researchers is the development of reliable methodologies to produce smaller size ranges of perovskite NPs, while keeping precise control over their composition, structural/crystal phase and shape, usually using non-aqueous sol-gel routes and water-free systems.

Such non-aqueous approaches have been developed by Karmaoui *et al*., among others,[32, 33] to produce a large variety of NPs including alkaline-earth/transition aluminates,[32, 34] various metal oxides[35] and hybrid materials.[36, 37] The method reported here, known as the "benzyl alcohol route", was first used to produce $SrHfO_3$ NPs in 2012 at a temperature of 300 °C. [38] However, the details of the synthesis route were never given, the NPs were not characterised in detail, and the formation mechanism was not investigated, as this paper focussed only on the photoluminescent characterisation of the $SrHfO_3$ NPs. Indeed, these NPs were synthesised by M. Karmaoui (see the acknowledgements of this article) from a benzyl alcohol route, and he has continued to optimise the process since then.

This paper details the benzyl alcohol route synthesis of perovskite-type $SrHfO_3$ nanomaterials at very low temperatures of 220 °C, much less than those of the other synthesis routes discussed above. Furthermore, this produced ultra-small nanocrystals of perovskite-type $SrHfO_3$, the smallest NPs even reported for this material. The NPs reported had a very small average diameter of 2.5 nm, a narrow log-normal size distribution, and an improved spherical shape, in comparison with other methods reported in the literature. For the first time the mechanism of formation of these $SrHfO_3$ NPs from the benzyl alcohol route was investigated, using NMR and GC-MS. This is also the first time the dielectric properties of $SrHfO_3$ NPs (as opposed to thin films or sintered ceramics) have been measured, an important feature, as previous studies of $SrHfO_3$ NPs

have focused only on their luminescent, and not dielectric, properties.

Experimental Methods

Strontium metal (99.99 %), hafnium isopropoxide (99.9 %) and anhydrous benzyl alcohol (99.8 %) were used without further purification, all supplied by Sigma Aldrich.

The synthesis was carried out in a glovebox (O_2 and H_2O < 1 ppm). In a typical synthesis of the strontium hafnium oxide nanocrystals, one mmol of metallic strontium (0.0876 gr) was dissolved in 20 mL of anhydrous benzyl alcohol. Once the solution became clear/dissolved (stirring at around 60 °C; 2 hours was needed to dissolve the metallic strontium), 1 mmol of hafnium isopropoxide (0.41484 gr) was added. The reaction mixture was transferred into a stainless steel autoclave, and carefully sealed to maintain anaerobic conditions. The autoclave was taken out of the glove-box, and heated in a furnace at 220 °C for 48 hours. The resulting milky suspensions were centrifuged, and the precipitates were thoroughly washed with ethanol, then dichloromethane, and then dried in air at 60 °C.

To uncover the formation mechanism, the reaction solution (supernatant) obtained by the centrifugation of the solid material was subjected to nuclear magnetic resonance (NMR) spectroscopy analysis. NMR was performed on a Bruker instrument at 300 MHz using $CDCl_3$ as the solvent. The sample was also analysed by gas chromatography – mass spectrometry (GC-MS) on a Trace Gas Chromatograph 2000 Series, equipped with a Thermo Scientific DSQ II single-quadrupole mass spectrometer (electron impact energy: 70 eV; collection rate: 1 scan s^{-1}; ion source temperature: 250 °C; m/z range: 33–700) and a DB-1 J&W capillary column (30 m x 0.32 mm inner diameter, 0.25 µm film thickness), using helium as carrier gas. The chromatographic conditions were as follows: initial temperature, 50 °C for 1 min; temperature gradient, 20 °C min^{-1}; final temperature, 250 °C; injector temperature, 270 °C; transfer-line temperature, 290 °C; split ratio, 1:33.

X-ray powder diffraction (XRPD) data were collected using a laboratory $\theta/2\theta$ diffractometer (PANalytical X'Pert Pro), equipped with a fast RTMS detector (PANalytical PIXcel 1D), with Cu K_α radiation (generated at 45kV and 40 mA, 15-115 °2θ range, a virtual step scan of 0.02 °2θ and virtual time per step of 500 s). The incident beam pathway was as follows: 0.125° divergence slit, 0.125° anti-scattering slit, 0.04 rad soller slits, and a 15 mm copper mask. The pathway of the diffracted beam included a Ni filter, soller slits (0.04 rad), and an antiscatter blade (5 mm). The crystal structural refinement, as well as a quantitative phase analysis (QPA) of the $SrHfO_3$ – taking solely into account the crystalline phases present in the sample – was assessed via the Rietveld method as implemented in the GSAS-EXPGUI software package.[39] $SrHfO_3$, depending on the temperature, is reported to undergo various structural transitions, but at room temperature, and consistent with Raman spectroscopic analyses, it crystallizes in the orthorhombic *Pbnm* type perovskite structure.[40] The starting atomic parameters for $SrHfO_3$, described in the space group (SG) *Pbnm*, were taken from Kennedy *et al*.,[16] and [41] those of metallic Sr (SG *Im3m*) from a work by McWhan and Jayaraman.[42] The instrumental contribution was obtained by refining the NIST SRM 660b standard (LaB_6). The following parameters were then refined: scale-factors, zero-point, 6 coefficients of the shifted Chebyshev function to fit the background, unit cell parameters, profile coefficients (one θ independent Gaussian term, G_w, and two Lorentzian terms, L_X and L_Y), atomic positions, and isotropic displacement parameters (U_{iso}) – after the first refinement cycles, U_{iso} values were constrained, so as to avoid negative values, that are physically meaningless, but are often obtained handling data of materials with limited coherence, i.e. nanocrystals.

The microstructural refinement was assessed on the same XRPD data, via the whole powder pattern modelling (WPPM) procedure, that allows for refinement of model parameters via a non-linear least squares procedure;[43, 44] such modelling was assessed by the PM2K software.[45]

WPPM is a state-of-the-art methodology that enables us to extract microstructural information from a diffraction pattern. In this way, the experimental peaks are fitted without any use of arbitrary analytical functions (like Gaussian, Lorentzian, or Voigtian functions), the diffraction peak profile being the result of a convolution of instrumental and sample-related physical effects. Consequently, the analysis is directly made in terms of physical models of microstructure and/or lattice defects. Hence, with the WPPM formalism, aspects of $SrHfO_3$ microstructure, such as the crystalline domain shape and size distribution, can be reliably studied, with much greater accuracy than possible with the integral breadth methods that are frequently used for line profile analysis (LPA), such as the routinely applied Scherer formula,[46] or the Williamson–Hall method.[47] In these latter methods,[40, 47] effects of the instrumental profile component, background and peak profile overlapping can make it very difficult to correctly extract integral breadths. Furthermore, additional sources of line broadening – i.e. domain size, lattice strain and layer faulting – cannot be considered properly.[48] Hence, it has to be stressed that the WPPM formalism is beyond Rietveld, and unlike the Rietveld method, it uses physical models of the microstructure to generate a theoretical expression of the line profiles – thus physically sound models for the microstructure are directly refined on the experimental data to provide self-consistent results. Fundamentally, WPPM technique describes each observed peak profile as a convolution of instrumental and sample-related physical effects, thus refining the corresponding model parameters directly on the observed data.[49, 50]

The instrumental contribution was obtained by modelling (using the same software) 14 *hkl* reflections from the NIST SRM 660b standard (LaB_6), according to the Caglioti *et al.* relationship.[51] Afterward, $SrHfO_3$ (SG *Pbnm*) and Sr (SG *Im3m*) were included in the WPPM modelling, and the following parameters were refined: background (modelled using a 6^{th}-order of the shifted Chebyshev polynomial function) peak intensities, lattice parameters, and specimen displacement. Crystalline domains were assumed to be spherical, and distributed according to a lognormal size distribution.

High-resolution scanning transmission electron microscopy (HRSTEM) experiments have been performed using a FEI Titan Low-Base microscope operated at 300 kV and equipped with a CESCOR C_s probe corrector, an ultra-bright X-FEG electron source and a monochromator. HRSTEM imaging was performed by using high-angle annular dark field (HAADF) detector; the inner and outer angles for most of the micrographs recorded were 48 and 200 mrad, respectively. Samples for HRSTEM investigations were prepared by dispersing the NPs in ethanol and evaporating the drops of the suspension on carbon-coated copper grids.

Diffuse reflectance spectroscopy (DRS) was used to assess the optical E_g of the NPs. Spectra were acquired in reflectance mode on a Jasco V-560 spectrometer, in the UV-Vis range (220–850 nm), with 0.5 nm step-size, using an integrating sphere and a white reference material, made of MgO. Optical band gap (E_g) of the material was obtained using the Tauc plot.[52,53] Literature data are contrasting regarding the type of $SrHfO_3$ transition: some authors report it to be directly allowed,[54] others that it is an indirectly allowed transition.[55] Hence, in this work, both cases were considered. Raman spectra were measured at room temperature using a micro-Raman spectrometer (Horiba Jobin Vyon) with a 633 nm excitation laser, an edge filter for Rayleigh line rejection, and a CCD detector. The laser was focused on the sample to a spot size of ~ 2 μm using a 50 x objective lens.

Dielectric measurements were carried out in the frequency range 100 Hz – 1 MHz at room temperature using an impedance analyser (Agilent 4294A). For this purpose, nanoparticles were pressed into a cylindrical pellet under hydrostatic pressure of 1 MPa. Capacitance was measured as a function of frequency and bias voltage, using a specially designed sample holder, placing the sample between platinum plates.

The photoluminescence spectra of as-synthesized $SrHfO_3$ NPs were recorded at room temperature with a modular double grating excitation spectrofluorimeter with a TRIAX 320 emission monochromator (Fluorolog-3, Horiba Scientific) coupled to a R928 Hamamatsu photomultiplier, using a front face acquisition mode. The excitation source was a 450 W Xe arc lamp. The emission spectra were corrected for detection and optical spectral response of the spectrofluorimeter, and the excitation spectra were corrected for the spectral distribution of the lamp intensity using a photodiode reference detector.

Results and discussion

The solvothermal process is a powerful route for preparing nanoparticles. We present a simple approach to synthesize $SrHfO_3$ nanocrystals with ultra-small crystal size. The synthesis of these perovskite nanocrystals involves the dissolution of metallic strontium in benzyl alcohol, after which hafnium isopropoxide was added, and the homogenous mixture was transferred to an autoclave and heated at 220 °C for 48 hrs. In order to get more insight into the formation mechanism of the $SrHfO_3$ NPs, liquid nuclear magnetic resonance (NMR) spectroscopy (^1H and ^{13}C) and coupled gas chromatography-mass (GC-MS) studies were performed on the organic species that remained after synthesis, in the supernatant isolated after centrifugation. ^{13}C NMR analysis of the supernatant confirmed the existence, in addition to benzyl alcohol, of significant amounts of other organic species. Remarkably, toluene, benzyl alcohol, 4-phenyl-2-butanone and 4-phenyl-2-butanol were the only species that could be observed as dominant compounds in the spectrum. In order to support these findings, GC-MS was carried out on the supernatant. GC-MS is simple and rapid, but very sensitive, tool for identification of complete organic compounds.

Significant amounts of several organic molecules resulting from the synthesis were detected, including dichloromethane, hexane, toluene, benzaldehyde, benzyl alcohol, 4-phenyl-2-butanol, 4-phenyl-2-butanone, 1,5-diphenyl-3-pentanol, 1,5-diphenyl-3-pentanone and benzyl ether, as well as other organic species in insignificant quantities (see more detail in table 1, Suppl. Info). Characteristic compounds identified with both NMR and GC-MS analyses were found to be outstanding accordance with reference spectra in the Integrated Spectral Data Base System for Organic Compounds. The knowledge gained from the identification of these organic species now permits to us to propose a reaction mechanism. We know that the non-aqueous sol-gel synthesis of $SrHfO_3$ nanocrystals is based on two consecutive steps which involve:

(a) the reaction of metallic strontium with benzyl alcohol to produce an alkoxide, with the release of hydrogen;[56]

(b) the reaction between the strontium benzyl alcoholate (alkoxide, formed upon dissolution of metallic strontium) and hafnium isopropoxide precursor results in the formation of multi metal oxide $SrHfO_3$ nanoparticles as proposed in scheme 1.

QPA data and Rietveld agreement factors are reported in Table1 (see more detail in table 1, Supp. Info). A graphical output of the Rietveld crystal structural refinement is depicted in Figure 1. The crystal structural data, as well as a 3D rendering of its crystal structure obtained with the VESTA software package,[57] inserting the structural data (bond lengths, bond angles, atomic positions and U_{iso}) obtained from GSAS, and reported in Table 1, are both shown in the inset of Figure 1.

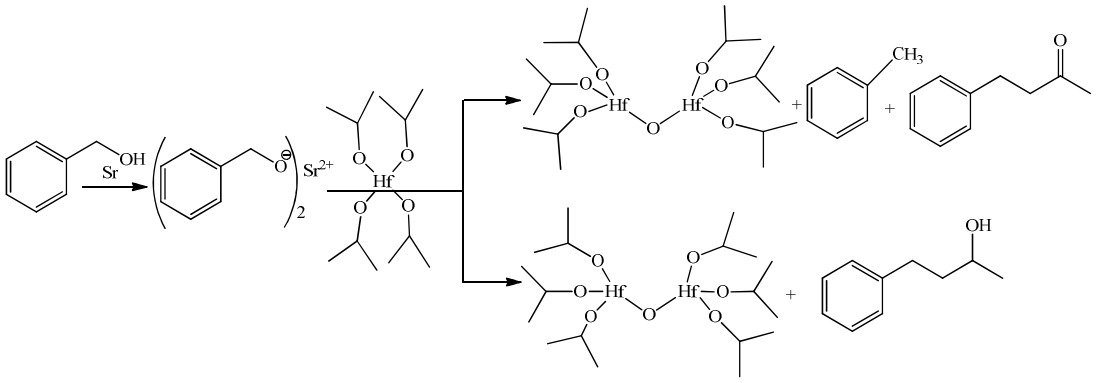

Scheme 1. Proposed reaction mechanism occurring during the non-aqueous synthesis of $SrHfO_3$ metal oxide nanoparticles in benzyl alcohol.

Journal Name

ARTICLE

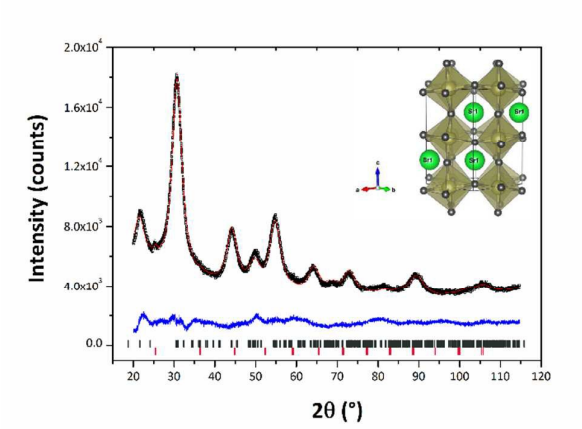

Figure 1. Graphic output of the Rietveld refinement of the $SrHfO_3$ sample. The black open squares represent the observed pattern, the continuous red line represents the calculated pattern, and the difference curve between observed and calculated profiles is the blue continuous line plotted below. The positions of reflections are indicated by the small vertical bars (dark grey = $SrHfO_3$, red = Sr). In the inset is reported a 3D rendering of the SrHfO3 crystal structure (space group, *Pbnm*). The small dark grey spheres represent oxygen, the larger dark green spheres are hafnium (coordination VI), whilst the largest, light green spheres are strontium (coordination X). Octahedral tilting of the perovskite (a−b+a−, using the Glazer's notation, as obtained using SPuDS software) can be appreciated from the 3D rendering.

As can be seen in Table 2, the sample is composed of 98.7 wt % $SrHfO_3$, with a small amount (1.3 wt %) remaining of the metallic Sr precursor, presumably as a result of incomplete dissolution in the benzyl alcohol.

Table 1 – Structural parameters for the $SrHfO_3$ phase (space group: *Pbnm*). Unit cell parameters of $SrHfO_3$, expressed in Å, were: a = 5.7108(30); b = 5.8245(36); c = 8.2248(42).

Atom	Site	Atomic position			Uiso
		x	y	z	(Å2 × 100)
Sr	4c	0.5300(1)	0.5412(1)	1/4	0.8(1)
Hf	4a	0	1/2	0	0.5(1)
O1	4c	0.4748(7)	−0.0161(8)	1/4	0.8(1)
O2	8d	0.7368(4)	0.2855(5)	0.0371(4)	0.6(1)

There were 7233 observations; the number of $SrHfO_3$ reflections in the data set was 402.

Table 2 – Agreement factors of the Rietveld refinement, and crystalline phase composition of the prepared sample.

No. of variables	Agreement factors				Crystalline phase composition (wt%)	
	$R(_F^2)$ (%)	R_{wp} (%)	χ^2		$SrHfO_3$	Sr
14	3.23	2.87	5.55		98.6(1)	1.4(1)

Structural parameters (atomic positions) calculated via the Rietveld refinement are in good agreement with those experimentally calculated through the SPuDS software,[58] cf Table 2 of the ESI. However, despite the good consistency of the obtained data, it is worth noting that, because of the very limited coherence in nanocrystals, complications may arise when investigating NPs, as the integrated intensities of Bragg's peaks can be determined only with large uncertainty because of the extremely broad profile. Hence, data in Table 1 are intended to be only relative. As a matter of fact, a local probe, as the pair distribution function (PDF), would be here necessary, aiming at highlighting the local differences, compared to the average structure that is obtainable from conventional crystallography. [59]

The size distributions were provided by an advanced X-ray powder diffraction (XRPD) technique, namely the whole powder pattern modelling (WPPM) method. The graphical output of the WPPM modelling of the as synthesized $SrHfO_3$ sample is shown in Figure 2 together with the crystalline domain size distribution.

The agreement factors and the microstructural data of WPPM modelling are reported in Table 3 of the ESI. From this advanced XRPD analysis, the average crystalline domain diameter of as-prepared $SrHfO_3$ NPs was found to be 2.5 nm, having a narrow size distribution, the mode being 2.0 nm, with little dispersion around the tails. Also, from Figure 2, it is interesting to note that there are no detected crystalline domains with diameters approximately < 0.7 and > 7.5 nm.

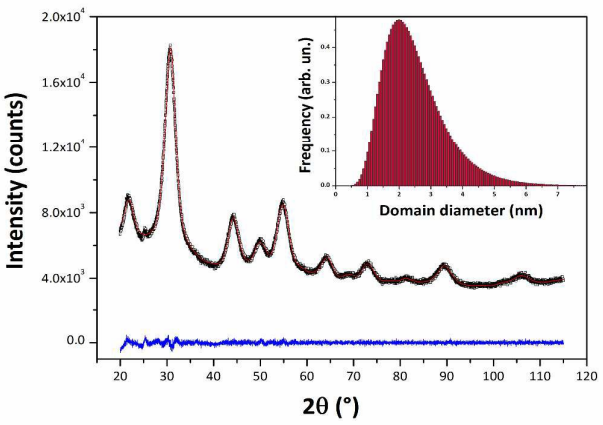

Figure 2. Graphic output of the WPPM modelling of the $SrHfO_3$ sample. The black open squares represent the observed pattern, the continuous red line represents the calculated pattern, and the difference curve between observed and calculated profiles is the blue continuous line plotted below. In the inset is reported the crystalline domain size distribution of $SrHfO_3$.

To check the consistency of the data extracted from X-ray analyses, detailed investigations at the sub-nanometer level of the perovskite $SrHfO_3$ NPs were performed by HRSTEM-HAADF experiments. Figure 3a) and b) provide a representative HRSTEM overview of the metal oxide perovskite-type $SrHfO_3$ nanoparticles. They are quite regular in shape with quasi-spherical morphology and the diameter of the NPs is estimated to be between 2 and 4 nm. This is good agreement with the data extracted from the XRD analyses in the WPPM formalism. The crystalline nature of the NPs is clearly seen in all the micrographs (see also the inset in figure 3a)) as-synthesized NPs. In order to investigate the structural phase of the NPs, interpretations of the Fourier Transform (FFT) patterns obtained on single NP (top inset of Figure 3b) were performed by using the JEMS software.[41] It is important to note that for all the NPs investigated, successful indexation of the FFTs was possible only by using the $SrHfO_3$ *Pbnm* type perovskite structure (top inset of Figure 3b) whereas no solution was found with the metallic Sr (SG *Im3m*) structure. These findings confirm the results obtained from X-ray analyses regarding the crystal structure of the $SrHfO_3$ NPs and the size distribution of the crystallites, as well as the low concentration of metallic Sr impurities in the synthesised products.

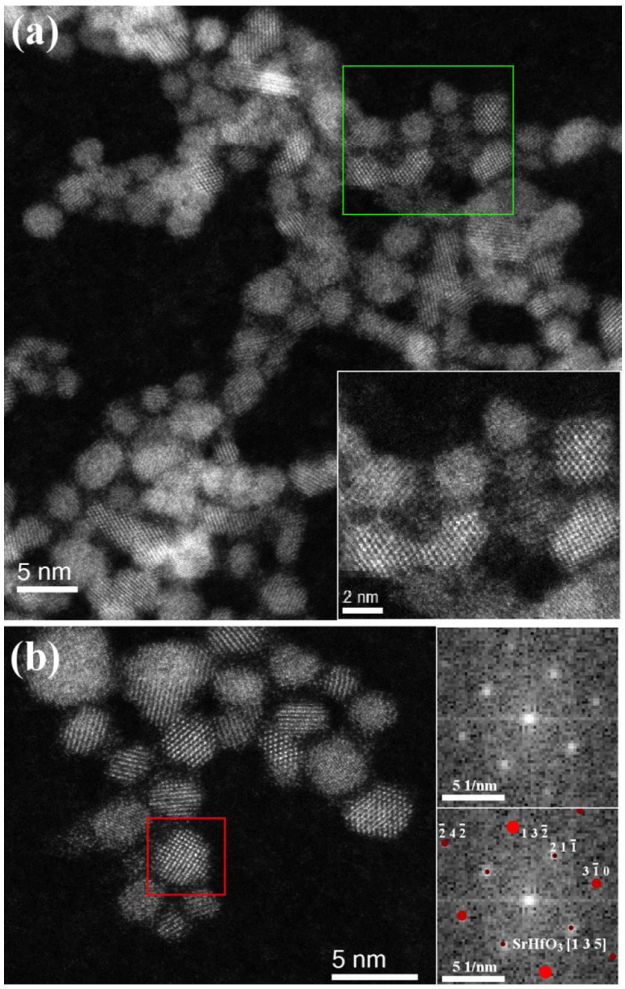

Figure 3. HRSTEM-HAADF micrographs of as-synthesized $SrHfO_3$ NPs. The Inset in *(a)* shows a magnified view of the area demarcated by the green square. The insets in *(b)* display the FFT pattern obtained from a single NP (red square) (*top*) and the superposition with the simulated diffractogram obtained with the $SrHfO_3$ *Pbnm* type perovskite structural data described in Table 1 in the [1 3 5] zone axis *(bottom).*

Raman spectroscopy is a sensitive technique for detecting small lattice distortions in the local crystal structure. We measured Raman spectra of as-synthesized, as well as annealed, $SrHfO_3$ NPs. The Raman spectrum of $SrHfO_3$ nanoparticles is shown in figure 4. The spectrum exhibits major peaks around 408, 549, 678 and 850 cm^{-1}, along with weak vibrations at 146, 167, 408, 617 and 830 cm^{-1}. The observation of these vibrational modes further substantiates the formation of single phase crystalline $SrHfO_3$ nanoparticles.

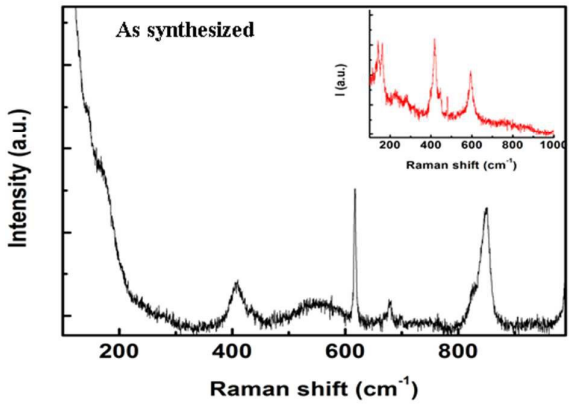

Figure 4. Raman spectrum of as-synthesized $SrHfO_3$ nanoparticles, and in the inset, those annealed at 800 °C.

According to literature, orthorhombic $SrHfO_3$ with the *Pbnm* space group exhibits 24 Raman active modes ($7_{Ag}+5B_{1g}+7B_{2g}+5B_{3g}$), 25 IR active modes ($9B_{1u}+7B_{2u}+9B_{3u}$) and 3 translational modes ($B_{1u}+B_{2u}+B_{3u}$).[19, 60, 61]

The observed peaks match well with literature, confirming the orthorhombic phase. Compared to the as-synthesized NPs, the sample annealed at 800 °C shows well defined bands around 141, 163, 418, 446, 594 cm^{-1}, which were assigned to the A_g, B_{1g}, A_g, B_{2g}, Ag modes, respectively, as well as minor peaks at 222, 280 and398 cm^{-1} corresponding to A_g, B_{3g} and B_{2g}. The assignment of Raman modes for different wavenumbers is done based on the theoretical work and recent experimental studies.[19, 62] The high frequency vibrational peaks around 830 and 850 cm^{-1} observed for as prepared samples correspond to B_{2g} and B_{3g} modes of orthorhombic phase. The observation of broad Raman peaks, and their shift towards higher wave numbers for $SrHfO_3$ NPs compared to the annealed samples, indicates the strain present in the lattice due to size effects. $SrHfO_3$ in general shows a variety of phase transitions: orthorhombic ➔ tetragonal ➔ cubic as temperature increases.[19] Here it can be noted that the size effect did not contribute to any structural change in the as-synthesized sample. Diffuse reflectance spectroscopy (DRS) data are reported in Figure 5a-c. Figure 5a shows the reflectance *versus* energy, whilst Figure 5b-c show the Tauc plot outputs, considering indirectly and directly allowed transitions, respectively. The results highlighted that, considering an indirectly allowed transition (Figure 5b), the optical E_g of our $SrHfO_3$ NPs is equal to 5.78 eV, consistent with the 5.7 eV value reported by Fursenko et al.[55]

The increase of such defects should promote an increase in the PL emission intensity. Thus, this emission band can be assigned to the attached benzoate complex molecules on the surface of the NPs, as already observed in our previous work.[37]

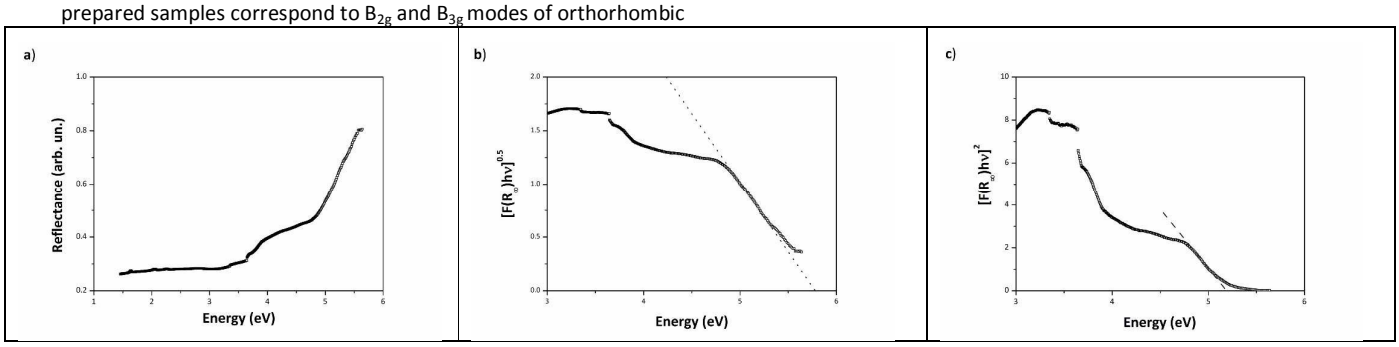

Figure 5. a) Diffuse reflectance spectrum of $SrHfO_3$ – reflectance *versus* energy. b) and c) show the Kubelka–Munk elaborations for the same sample. In b), the dotted line represents the *x*-axis intercept of the line tangent to the inflection point, *e.g.* its apparent optical E_g (5.78 eV), calculated with the Tauc procedure, and assuming the transition to be **indirectly allowed** (power coefficient γ = ½). In c), the dashed line represents the *x*-axis intercept of the line tangent to the inflection point, *e.g.* its apparent optical E_g (5.20 eV), calculated with the Tauc procedure, and assuming the transition to be **directly allowed** (power coefficient γ = 2).

Journal Name

ARTICLE

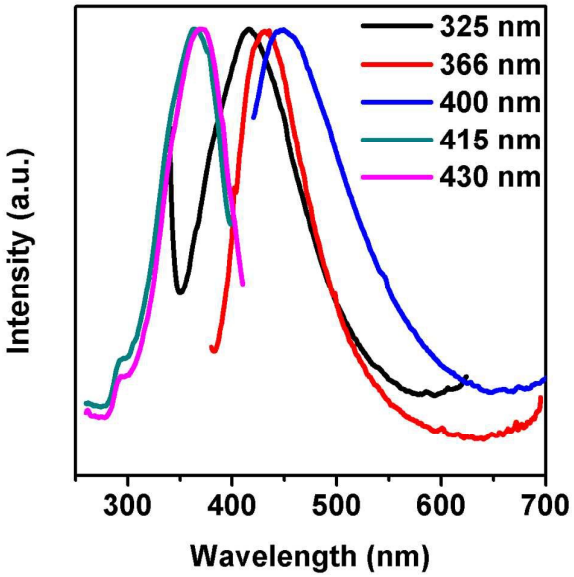

Figure 6. Room temperature emission spectra of pure $SrHfO_3$ excited at 325, 366, 400, 415 and 430 nm.

Under excitation wavelengths in the range of 415–430 nm, two broad UV components appear at 366 and 290 nm positions, in which the large band at 366 nm represents the benzoate-related emission, and the lower intensity 290 nm band is probably related to the host $SrHfO_3$ NPs. The PL emission in these perovskite NPs, at room temperature, is thus controlled by the structure and the degree of disorder. Such structural disorder will result in a non-uniform band gap structure in which electrons or holes may be trapped.

To study the dielectric properties of our $SrHfO_3$ NPs, we measured capacitance as a function of frequency and voltage. For this purpose, a thin pellet of $SrHfO_3$, with an area of 200 x 200 μm, sandwiched between platinum plates, was used for measurements.

The frequency dependence of capacitance measured at room temperature is shown in figure 7(a). The data shows narrow frequency dispersion within the measured frequency range, similar to that reported in literature for $SrHfO_3$ thin films. The calculated value of relative permittivity is 17 at 100 kHz, which is slightly smaller compared to a reported value of 21 for 59 nm thick $SrHfO_3$ films grown on Si by atomic layer deposition.[63] Bulk sintered $SrHfO_3$ ceramics were reported to have a relative permittivity of 23.5 at 9.3 GHz [11], and sintered NPs made from a combustion route had a value of 25 at 1 MHz, so our unsintered and unannealed (as-prepared) NPs compare very well.

It is commonly known that the dielectric parameters are a function of grain size, and hence, this observed value is reasonable for such nanoscaled grains as we have in our sample. Here it is noteworthy to mention that the influence of small hydrostatic pressure (1MPa) is insignificant for present dielectric properties as most of the effects observed on nanoparticles were reported at high pressures.[64, 65] For example, $BaTiO_3$ nanoparticles experience a reduction in phase transition temperature (at a rate of 34.3K/GPa) and large change in permittivity at hydrostatic pressures above 200 MPa.[64]

The room temperature dielectric loss (tan δ) shows a decreasing trend with frequency, as is to be expected, possessing a value in the range 0.7-0.5 for frequencies up to 1 kHz, with the losses levelling out above 10 kHz, with a value of 0.02 at 100 kHz and around the same at 1 MHz. These values are one order larger compared to those reported for $BaHfO_3$ perovskites.[66] Figure 7b shows the C-V (capacitance-voltage) curve for the $SrHfO_3$ NPs measured at 100 kHz. The value of C_{max} is 3.837 pF that corresponds to a relatively larger value of 9.55 nF cm^{-2}. It can be noticed that capacitance displays a narrow hysteresis loop with a narrow opening (ΔV = 2.1V). Such a hysteresis is an indication of dipole rotation of crystalline domains when a high electric field of opposite polarity is applied (a complete saturation was not possible in the present study due to constraints of applied voltage). There have been speculations that $SrHfO_3$ satisfies the soft mode conditions to become a displacive ferroelectric.[19] However, further studies are required to find out the origin of such hysteresis behaviour.

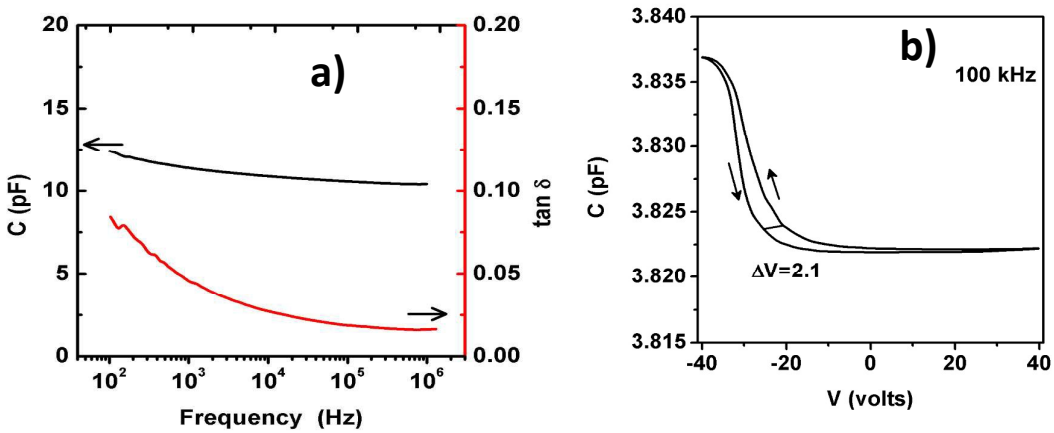

Figure 7. a) Frequency and b) bias voltage dependence of capacitance.

Conclusions

The non-aqueous sol-gel solution-phase synthesis of $SrHfO_3$ nanocrystals performed in this study is a promising route that had not been investigated previously. A one-pot synthesis to prepare perovskite-type $SrHfO_3$ nanocrystals, at low temperature, with ultra-small size, and spherical morphology, is presented. Quantitative XRPD microstructural analysis, via the WPPM method – used for the first time in the perovskite system – and HRSTEM gave detailed information about the size, size distribution and shape of the $SrHfO_3$ NPs, which are nanocrystals around 2.5 nm in diameter. A possible mechanism for the formation of the perovskite $SrHfO_3$-type oxide nanoparticles was also proposed and discussed, based on the results of NMR and GC-MS, proceeding via the condensation of two metal alkoxide molecules, leading to the formation of Hf–O–Hf bridges. Capacitance measurements indicated a dielectric constant of 17, which is reasonably high for a nanoscaled material, and compares to the reported value of 21 in the case of larger grain sized $SrHfO_3$. The measured capacitance was 9.5 nF cm^{-2}. Therefore, we verified that $SrHfO_3$ NPs could be a potential dielectric material which could serve as a gate in FET applications.

Acknowledgements

Mohamed Karmaoui thanks Fundação para a Ciência e a Tecnologia (FCT) for Grant no. SFRH/BPD/74477/2010. Robert C. Pullar acknowledges the support of FCT grant SFRH/BPD/97115/2013. This work was developed in the scope of the project CICECO-Aveiro Institute of Materials (Ref. FCT UID /CTM /50011/2013), financed by national funds through the FCT/MEC and when applicable co-financed by FEDER under the PT2020 Partnership Agreement. Mohamed Karmaoui thanks Prof. Artur Silva for NMR measurements and fruitful discussions. Dr Carla Andrea Vilela is acknowledged for helpful discussions regarding the GC-MS (University of Aveiro, Portugal). Authors also acknowledge the PEstC/CTM/LA0011/2013 programme. E. Venkata Ramana would like to acknowledge the financial support from FCT, Portugal (SFRH/BPD/75582/2010). The HRSTEM work was conducted in the Laborario de Microscopías Avanzadas (LMA) at the Instituto de Nanociencia de Aragón (INA) - Universidad de Zaragoza (Spain). Some of the research leading to these results has received funding from the European Union Seventh Framework Program under Grant Agreement 312483 - ESTEEM2 (Integrated Infrastructure Initiative – I3). Raul Arenal also acknowledges funding from the Spanish Ministerio de Economia y Competitividad (FIS2013-46159-C3-3-P).

References

1. J. Suntivich, K. J. May, H. A. Gasteiger, J. B. Goodenough and Y. Shao-Horn, *Science*, 2011, **334**, 1383-1385.
2. S. Royer, D. Duprez, F. Can, X. Courtois, C. Batiot-Dupeyrat, S. Laassiri and H. Alamdari, *Chem. Rev.*, 2014, **114**, 10292-10368.
3. W. J. Schipper, J. J. Piet, H. J. De Jager and G. Blasse, *Mater. Res. Bull.*, 1994, **29**, 23-30.
4. E. Mihóková, N. Chiodini, M. Fasoli, A. Lauria, F. Moretti, M. Nikl, V. Jarý and A. Vedda, *Phys. Rev. B*, 2010, **82**, 165115.
5. A. Atkinson, S. Barnett, R. J. Gorte, J. T. S. Irvine, A. J. McEvoy, M. Mogensen, S. C. Singhal and J. Vohs, *Nat Mater*, 2004, **3**, 17-27.
6. J. Suntivich, H. A. Gasteiger, N. Yabuuchi, H. Nakanishi, J. B. Goodenough and Y. Shao-Horn, *Nat Chem*, 2011, **3**, 546-550.
7. E. V. van Loef, Y. Wang, S. R. Miller, C. Brecher, W. H. Rhodes, G. Baldoni, S. Topping, H. Lingertat, V. K. Sarin and K. S. Shah, *Opt. Mater.*, 2010, **33**, 84-90.
8. H. Rétot, A. Bessière, A. Kahn-Harari and B. Viana, *Opt. Mater.*, 2008, **30**, 1109-1114.
9. G. Blasse, *Chem. Mater.*, 1994, **6**, 1465-1475.
10. C. Rossel, M. Sousa, C. Marchiori, J. Fompeyrine, D. Webb, D. Caimi, B. Mereu, A. Ispas, J. P. Locquet, H. Siegwart, R. Germann, A. Tapponnier and K. Babich, *Microelectron. Eng.*, 2007, **84**, 1869-1873.
11. 1992.
12. N. Arai, T. W. Kim, H. Kubota, Y. Matsumoto and H. Koinuma, *Appl. Surf. Sci.*, 2002, **197–198**, 402-405.
13. M. D. McDaniel, C. Hu, S. Lu, T. Q. Ngo, A. Posadas, A. Jiang, D. J. Smith, T. Y. Edward, A. A. Demkov and J. G. Ekerdt, *J. Appl. Phys.*, 2015, **117**, 054101.
14. A. Feteira, D. C. Sinclair, K. Z. Rajab and M. T. Lanagan, *J. Am. Ceram. Soc.*, 2008, **91**, 893-901.

15. M. Shinji, M. Yukinori, M. Meishoku and O. Hiroyuki, *Japanese Journal of Applied Physics*, 2014, **53**, 04EA03.
16. B. Kennedy, C. Howard and B. Chakoumakos, *Phys. Rev. B*, 1999, **60**, 2972-2975.
17. C. Rossel, B. Mereu, C. Marchiori, D. Caimi, M. Sousa, A. Guiller, H. Siegwart, R. Germann, J.-P. Locquet, J. Fompeyrine, D. J. Webb, C. Dieker and J. W. Seo, *Appl. Phys. Lett.*, 2006, **89**, 053506
18. S. Shamuilia, V. V. Afanas'ev, A. Stesmans, I. McCarthy, S. A. Campbell, M. Boutchich, M. Roeckerath, T. Heeg, J. M. J. Lopes and J. Schubert, *J. Appl. Phys.*, 2008, **104**, 114103.
19. M. K. Singh, G. Singh, T. H. Kim, S. Kojima, R. S. Katiyar and J. F. Scott, *EPL (Europhysics Letters)*, 2014, **107**, 26004.
20. L. Wachowski, *Surf. Coat. Technol.*, 1986, **29**, 303-311.
21. P. K. Gallagher, D. W. Johnson Jr and F. Schrey, *Mater. Res. Bull.*, 1974, **9**, 1345-1352.
22. M. S. G. Baythoun and F. R. Sale, *Journal of Materials Science*, 1982, **17**, 2757-2769.
23. L. G. Tejuca, J. L. G. Fierro and J. M. D. Tascón, in *Advances in Catalysis*, eds. H. P. D.D. Eley and B. W. Paul, Academic Press, 1989, vol. Volume 36, pp. 237-328.
24. Y. Yang, S. Priya, Y. U. Wang, J.-F. Li and D. Viehland, *J. Mater. Chem.*, 2009, **19**, 4998-5002.
25. X. Yang, Z. Ren, G. Xu, C. Chao, S. Jiang, S. Deng, G. Shen, X. Wei and G. Han, *Ceram. Int.*, 2014, **40**, 9663-9670.
26. D. R. Modeshia and R. I. Walton, *Chem. Soc. Rev.*, 2010, **39**, 4303-4325.
27. P. Boháček, B. Trunda, A. Beitlerová, J. Drahokoupil, V. Jarý, V. Studnička and M. Nikl, *J. Alloys Compd.*, 2013, **580**, 468-474.
28. J. K. Thomas, J. Koshy, J. Kurian, Y. P. Yadava and A. D. Damodaran, *J. Appl. Phys.*, 1994, **76**, 2376-2379.
29. J. K. Thomas, H. Padma Kumar, S. Solomon, K. C. Mathai and J. Koshy, *J. Alloys Compd.*, 2010, **508**, 532-535.
30. Ł. John and P. Sobota, *Acc. Chem. Res.*, 2014, **47**, 470-481.
31. T. Ye, Z. Dong, Y. Zhao, J. Yu, F. Wang, L. Zhang and Y. Zou, *Dalton Transactions*, 2011, **40**, 2601-2606.
32. M. Karmaoui, N. J. O. Silva, V. S. Amaral, A. Ibarra, A. Millan and F. Palacio, *Nanoscale*, 2013, **5**, 4277-4283.
33. M. Karmaoui, M. G. Willinger, L. Mafra, T. Herntrich and N. Pinna, *Nanoscale*, 2009, **1**, 360-365.
34. M. Karmaoui, M.-G. Willinger, L. Mafra, T. Herntrich and N. Pinna, *Nanoscale*, 2009, **1**, 360.
35. N. Pinna and M. Niederberger, *Angewandte Chemie International Edition*, 2008, **47**, 5292-5304.
36. N. Pinna, G. Garnweitner, P. Beato, M. Niederberger and M. Antonietti, *Small*, 2005, **1**, 112-121.
37. M. Karmaoui, R. A. Sá Ferreira, A. T. Mane, L. D. Carlos and N. Pinna, *Chem. Mater.*, 2006, **18**, 4493-4499.
38. E. Rauwel, A. Galeckas, P. Rauwel and H. Fjellvåg, *Adv. Funct. Mater.*, 2012, **22**, 1174-1179.
39. A. C. Larson and R. B. V. Dreele, ed. L. A. N. Laboratory, Los Alamos, 2004, vol. LAUR 86-748
40. R. Vali, *Solid State Commun.*, 2008, **148**, 29-31.
41. P. Stadelmann, JEMS-SAAS, 2014.
42. D. B. McWhan and A. Jayaraman, *Appl. Phys. Lett.*, 1963, **3**, 129-131.
43. P. Scardi and M. Leoni, *Acta Crystallographica Section A*, 2002, **58**, 190-200.
44. Scardi P. and Leoni M., ed. E. J. Mittemeijer, Berlin, 2004, pp. 51–92.
45. M. Leoni, T. Confente and P. Scardi, *ZEITSCHRIFT FUR KRISTALLOGRAPHIE*, 2006, **23**, 249-254.
46. Klug HP. and Alexander LE., *X-Ray Diffraction Procedures: For Polycrystalline and Amorphous Materials- 2nd Edition. X-Ray Diffr Proced Polycryst Amorph Mater 2nd Ed Harold P Klug Leroy E Alexander*, 1974.
47. G. K. Williamson and W. H. Hall, *Acta Metall.*, 1953, **1**, 22-31.
48. P. Scardi and M. Leoni, *Acta Mater.*, 2005, **53**, 5229-5239.
49. P. Scardi and M. Leoni, in *Whole Powder Pattern Modelling: Theory and Applications. In Diffraction Analysis of the Microstructure of Materials;* , eds. Eric J. Mittemeijer and P. Scardi, Springer Series in Materials Science, 2004, vol. 68, pp. 51-92.
50. P. Scardi and M. Leoni, *J. Appl. Crystallogr.*, 2006, **39**, 24-31.
51. G. Caglioti, A. Paoletti and F. P. Ricci, *Nuclear Instruments and Methods*, 1960, **9**, 195-198.
52. J. Tauc, *Mater. Res. Bull.*, 1968, **3**, 37-46.
53. M. Karmaoui, D. M. Tobaldi, S. Andrijana Sever, R. C. Pullar, M. P. Seabra, J. A. Labrincha and V. S. Amaral, *RSC Advances*, 2014, **4**, 46762-46770.
54. L.-p. Feng, Z.-t. Liu, Q.-j. Liu and H. Tian, *Computational Materials Science*, 2010, **50**, 454-458.
55. O. Fursenko, J. Bauer, G. Lupina, P. Dudek, M. Lukosius, C. Wenger and P. Zaumseil, *Thin Solid Films*, 2012, **520**, 4532-4535.
56. R. C. Mehrotra, A. Singh and S. Sogani, *Chem. Soc. Rev.*, 1994, **23**, 215-225.
57. K. Momma and F. Izumi, *J. Appl. Crystallogr.*, 2008, **41**, 653-658.
58. M. W. Lufaso and P. M. Woodward, *Acta Crystallographica Section B*, 2001, **57**, 725-738.
59. V. Petkov, M. Gateshki, M. Niederberger and Y. Ren, *Chem. Mater.*, 2006, **18**, 814-821.
60. R. O. Kagel, R. A. Koster and W. T. Allen, *Appl. Spectrosc.*, 1976, **30**, 350-351.
61. M. K. Singh, N. K. Karan, R. S. Katiyar, J. F. Scott and H. M. Jang, *J. Phys.: Condens. Matter*, 2008, **20**, 055210.
62. A. Yangthaisong, *J. Electron. Mater.*, 2013, **42**, 993-998.
63. K. Black, M. Werner, R. Rowlands–Jones, P. R. Chalker and M. J. Rosseinsky, *Chem. Mater.*, 2011, **23**, 2518-2520.
64. J. Zhu, C. Jin, W. Cao and X. Wang, *Appl. Phys. Lett.*, 2008, **92**, 242901.
65. L. Shengtao, W. Weiwang, Y. Shihu and S. Huigang, *Dielectrics and Electrical Insulation, IEEE Transactions on*, 2014, **21**, 519-528.
66. J. K. Thomas, H. P. Kumar, V. S. Prasad and S. Solomon, *Ceram. Int.*, 2011, **37**, 567-571.

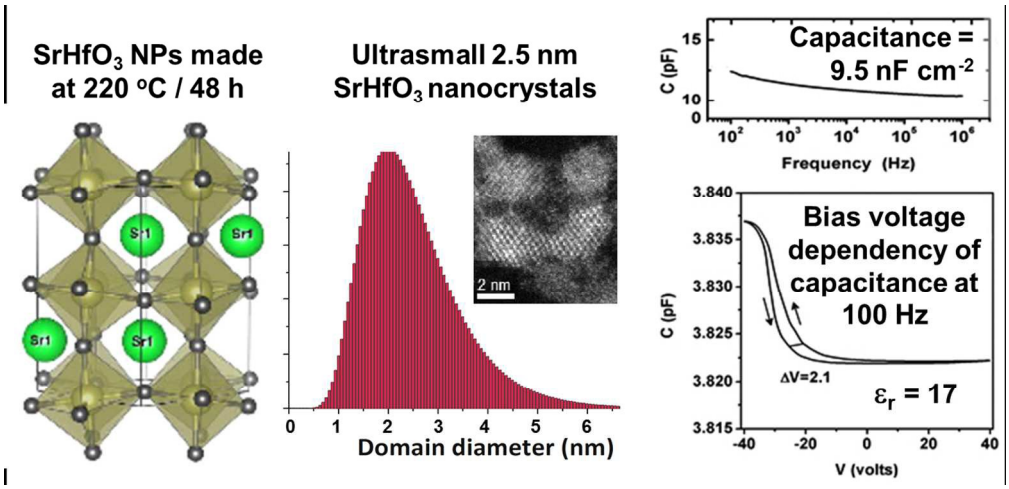

232x111mm (150 x 150 DPI)